A Superresolution Framework for fMRI Sequences and Its Impact on Resulting Activation Maps

P. Kornprobst[1], R. Peeters[2], M. Nikolova[3], R. Deriche[1], M. Ng[4], and P. Van Hecke[2]

[1] INRIA Sophia Antipolis, Projet Odyssée, France
[2] Department of Radiology, KULeuven, Belgium
[3] Département Traitement du Signal, ENST, Paris, France
[4] Department of Mathematics, The University of Hong Kong, Pokfulam, Hong Kong

Abstract. This paper investigates the benefits of using a superresolution approach for fMRI sequences in order to obtain high-quality activation maps based on low-resolution acquisitions. We propose a protocol to acquire low-resolution images, shifted in the slice direction, so that they can be used to generate superresolution images. Adopting a variational framework, the superresolution images are defiend as the minimizers of objective functions. We focus on edge preserving regularized objective functions because of their ability to preserve details and edges. We show that applying regularization only in the slice direction leads more pertinent solutions than 3-dimensional regularization. Moreover, it leads to a considerably easier optimization problem. The latter point is crucial since we have to process long fMRI sequences. The solutions—the sought high resoltion images—are calculated based on a half-quadratic reformulation of the objective function which allows fast minimization schemes to be implemented. Our acquisition protocol and processing technique are tested both on simulated and real functional MRI datasets.

1 Introduction

In functional Magnetic Resonance Imaging (fMRI) a major goal is to maximize the image spatial resolution, which will allow the investigator to visualize the smallest region of neuronal brain activity. In order to obtain high-resolution activation maps, the spatial resolution of the standard fMRI experiments performed at 1.5 T does not suffice, as the penalty for acquiring higher resolution images is a reduction in SNR [10] which is proportional to the decrease in voxel size. This decrease in SNR can be obviated by the use of higher magnetic field scanners [19], these however imply much higher equipment costs, an increased inhomogeneity and larger distortion artifacts in the images [7,12]. To overcome these problems, one possible solution is to use superresolution techniques which allows us to generate a high resolution volume from a set of low resolution ones. These techniques have already been used in different image processing applications [18,1,5,4,11]. For anatomical MR images, superresolution can be employed in 2D FT MR imaging in the image space, i.e. in the slice direction [9,15] and [16] proposed a superresolution approach for 3D volumes.

In this paper we consider fMRI time series and propose an optimized approach for high resolution fMRI images reconstructions. It is based on two parts. The first is the

R.E. Ellis and T.M. Peters (Eds.): MICCAI 2003, LNCS 2879, pp. 117–125, 2003.
© Springer-Verlag Berlin Heidelberg 2003

acquisition protocol (section 2). Images are acquired at a low resolution using alternate shifts of the image slice stack over half-a-slice thickness, generating two separate slice-shifted overlapping volumes. The second is the superresolution reconstruction technique which combines recent work on edge preserving approaches and convergence rate studies [14] (section 3). Section 4 presents the experiments on a synthetic sequence and on a real acquisition made on human volunteer for a visual stimulus. The properties of the resulting statistical parameter maps will be analyzed.

2 An Adapted fMRI Sequence

High resolution anatomical MRI images are classically acquired as 3D volumes. However the acquisition takes too much time and cannot reach the temporal resolution required in fMRI experiments. Instead MRI volumes are acquired as a stack of 2D slices perpendicular to a given direction (see figure 1). The in-plane image data of a single slice are generated by a 2D Fourier transform of the acquired set of MRI time-domain signals. In-plane shifting in the image space (which is nothing else than a global phase shift in the acquisition space), does not add any new information since due to the properties of the 2D inverse Fourier Transform, it is equivalent to zero-padding of the raw data in the temporal domain [9]. Therefore in fMRI, the use of a superresolution algorithm will be only beneficial in the slice direction (perpendicular to the image plane), since shifted slices correspond to different parts of the object in the real space.

Our acquired images are shifted only in the slice direction. According to our fMRI acquisition protocol, both volumes are acquired in an interleaved fashion with the first volume (G1) positioned with a relative slice offset equal to zero, and the second volume (G2) with a relative slice offset (Dz) of half the slice thickness, as is demonstrated in figure 1.

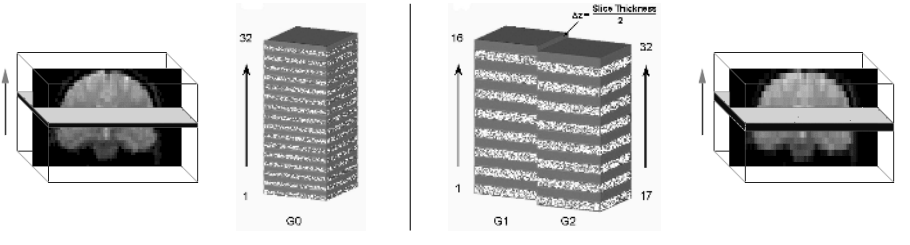

Fig. 1. The acquisition of the different slices in a volume. Left : The slice acquisition sequence in the standard high resolution dataset (G0). Right : The acquisition sequence in the slice shifted low resolution datasets (G1 and G2).

3 An Edge-Preserving Supperresolution Technique

Let us denote by Δ_x, Δ_y, Δ_z, the high resolution discretization steps (voxel dimensions). Each voxel $h_{i,j,k}$ represents the intensity of the image over the volume

$$W_{i,j,k} = [(i-1)\Delta_x, i\Delta_x] \times [(j-1)\Delta_y, j\Delta_y] \times [(k-1)\Delta_z, k\Delta_z]$$

Our low resolution images are denoted by l^r, for $r = 1, \ldots, R$. Each image l^r represents the the intensity of the image over the volume

$$V^r_{i,j,k} = [(i-1)\Delta_x, i\Delta_x] \times [(j-1)\Delta_y, j\Delta_y] \times [(R(k-1)+r)\Delta_z, (Rk+r))\Delta_z].$$

In [9] applying [11], a convolutional model is used to describe the relation between W and V. Instead, we adopt an additive model. If $s(x)$ is the signal intensity of the nuclei located at x, the signal relevant to a volume v is $\int_v s(x)dx$. The measurement noise involved in the data is denoted n. Thus we have

$$l^r_{i,j,k} = \sum_{n=R(k-1)+r+1}^{Rk+r} \int_{V_{i,j,n}} s(x)\, dx + n^r_{i,j,k} = \sum_{n=R(k-1)+r+1}^{Rk+r} h_{i,j,n} + n^r_{i,j,k} \quad (1)$$

This relation can be put into matrix form. Given (i, j), let $\mathrm{h}_{i,j}$ and $\ell^r_{i,j}$ be the vectors

$$\mathrm{h}_{i,j} = [h_{i,j,1}, \ldots, h_{i,j,p}]^T \quad (2)$$

$$\ell^r_{i,j} = [\ell_{i,j,1}, \ldots, \ell_{i,j,p_r}]^T \quad \text{for} \quad r = 0, \ldots, R-1 \quad (3)$$

where p_r is the length of $\ell^r_{i,j}$. The relation (1) can be expressed as

$$\ell^r_{i,j} = B^r \mathrm{h}_{i,j} + n^r_{i,j}, \ \forall i, j \quad \text{with} \quad B^r_{k,n} = \begin{cases} 1 & \text{if } R(k-1)+r+1 \le n \le Rk+r \\ 0 & \text{otherwise.} \end{cases}$$

The super-resolution problem consists in finding $\mathrm{h}_{i,j}$, for all i, j, based on $\ell^r_{i,j}$, for all r and i, j. The least-square solution of this problem is the minimizer $\hat{\mathrm{h}}$ of the following objective:

$$\Psi(h) = \sum_{i,j} \sum_{r=0}^{R-1} \left\| B^r \mathrm{h}_{i,j} - \ell^r_{i,j} \right\|^2. \quad (4)$$

Our problem (4) being ill-posed, such a $\hat{\mathrm{h}}$ is poor and unstable with respect to noise [4]. In such cases, a common approach in the field of computer vision is to add a penalty term on the first derivatives of h [4,6]. The sought solution is defined as the minimizer $\mathrm{h}h$ of a cost-function of the form

$$\mathcal{J}(h) = \Psi(h) + \Phi(h) \quad \text{where} \quad (5)$$

$$\Phi(h) = \sum_{i,j,k} \beta_x \phi(h_{i,j,k} - h_{i-1,j,k}) + \beta_y \phi(h_{i,j,k} - h_{i,j-1,k}) + \beta_z \phi(h_{i,j,k} - h_{i,j,k-1}) \quad (6)$$

The differences between the parentheses above provide an approximation of the spatial derivatives in the x, y and z-directions, and $\phi : R \to R$ is called a potential function. In

order to have a convex minimization problem, we require that ϕ be a convex function. Edge-preserving convex functions ϕ have been considered by many authors [17,8,3,2]. Among them, we chose

$$\phi(t) = \begin{cases} t^2/2 & \text{if } |t| \leq \alpha, \\ \alpha|t| - \alpha^2/2 & \text{if } |t| > \alpha. \end{cases} \qquad \text{(Huber function)} \tag{7}$$

because it is composed of quadratic and linear pieces and leads to simple numerical calculations. In our case, the acquisition procedure combines data only in the z-direction. This suggests we use regularization only along the z-axis, that is

$$\Phi(h) = \beta \sum_{i,j,k} \phi(h_{i,j,k} - h_{i,j,k-1}) = \beta \sum_{i,j} \sum_{k} \phi(\mathrm{h}_{i,j}(k) - \mathrm{h}_{i,j}(k-1)) \tag{8}$$

where we use the notation introduced in (2). The optimization problem is simplified to a sequence of 1-D minimizations, namely $\hat{\mathrm{h}}_{i,j} = \arg\min_{\mathrm{h}} J_{i,j}(\mathrm{h})$ for every i, j, where

$$J_{i,j}(\mathrm{h}) = \sum_{r=0}^{R-1} \left\| B^r \mathrm{h} - \ell_{i,j}^r \right\|^2 + \beta \sum_{k} \phi(\mathrm{h}(k) - \mathrm{h}(k-1)). \tag{9}$$

There are a lot of convergent methods to calculate $\hat{\mathrm{h}}$. However, based on a comparative study on the speed of convergence [14], we focus on the additive form of half quadratic regularization [8,3]. It amounts to calculate the sequence (h^n, b^n) as given below:

$$\mathrm{h}^n = H^{-1}(2B^T \ell_{ij} + \beta D^T b^n) \quad \text{where} \quad H = 2B^T B + \beta D^T D$$
$$b_k^n = \begin{cases} 0 \quad \text{if} \quad |\mathrm{h}^{n-1}(k) - \mathrm{h}^{n-1}(k-1)| \leq \alpha \\ \mathrm{h}^{n-1}(k) - \mathrm{h}^{n-1}(k-1) - \alpha \,\mathrm{sign}\,(\mathrm{h}^{n-1}(k) - \mathrm{h}^{n-1}(k-1)) \quad \text{otherwise} \end{cases}, \forall k$$

The sequence (h^n, b^n) converges to a $(\hat{\mathrm{h}}, \hat{b})$ such that $\hat{\mathrm{h}}$ is the sought solution. Observe that the matrix H can be inverted only once, before to start the minimization for all i, j and that calculation of b^n is extremely simple.

4 Experiments

The Two fMRI Datasets Used for the Evaluation

► A synthetized dataset sequence generated in *Matlab*. It consists of a template MR image with a base resolution of 3×3×4 mm^3. From this volume a dynamic time series of 120 volumes, was generated with different "activated spheres" inserted in an interleaved mode of 10 *rest* volumes and 10 *activated volumes*. These activated regions consisted of different spheres with different radii and carefully chosen positions. Another activated area consisted of an irregular shape at the edge of the brain. The intensity of the activation was set to a maximum of 8 percent signal change. In order to obtain a more realistic dataset, Gaussian noise was inserted with a standard deviation of 2 percent for the original high resolution set and 1 percent for the low resolution ones.

► A real fMRI experiment with a neurophysiological stimulation paradigm. Two different acquisition strategies were used in this experiment, the high and low resolution fMRI acquisition protocols (that is ground truth and slice-shifted). The stimuli used in the experiment were designed to stimulate the horizontal (HM) and vertical (VM) visual field meridian, using horizontally and vertically oriented wedge-shaped checkerboards. In this experiment a total of 10 sessions were performed on the same subject, consisting of 5 high resolution (ground truth) and 5 slice-shifted low resolution volume sessions. These data were collected on a Siemens Sonata 1.5T MR system using a FE-EPI sequence (TR/TE = 3328ms/54ms, voxel size = $2\times2\times2$ mm for the ground truth images and $2\times2\times4$ mm for the slice shifted images, acq. matrix = 128×128).


Low and high resolution datasets including the ones presented here are available at http://www-sop.inria.fr/odyssee/team/Pierre.Kornprobst/mridata

Postprocessing of the fMRI Data

The postprocessing of the functional MR images is performed with the aid of the SPM99 package (Friston et al, 1995). Images were first motion compensated with respect to the first image of the serie and spatially smoothed with an isotropic Gaussian kernel of $(3\ \text{mm})^3$. These preprocessing steps were identical for all the datasets (high resolution and superresolution) of the real fMRI experiment, for the synthetic data no preprocessing was perfomed. After these preprocessing steps the actual statistical analysis was performed on the different datasets (real and synthetic). As a result of the loss of the temporal information in the slice-shifted acquisition mode of the data, it was not possible anymore to use the standard SPM statistical analysis protocols for the superresolution datasets. Due to the properties of the haemodynamic response, the image data acquired during the initial and final portion of the task are not in a stationary state (plateau) and therefore these cannot be used for the post-hoc superresolution algorithm which should only combine two sets of shifted and non-shifted volumes acquired with an identical neurophysiological activation condition. A possible solution to use the full dataset and the hemodynamic response function in the analysis would be to use an acquisition time correction for all the separate slices on both the low resolution datasets before generating the superresolution datasets. In this study we chose to analyse the superresolution fMRI data with an adapted suboptimal design matrix by using the box-car function only, thus without taking into account the temporal properties of the fMRI signal.

Results and Discussion

► Approaches tested. The aim is to evaluate the approaches which consist in minimizing the energy (5), either with (6), a *3D regularization*, or with (8), a *1D regularization*. Results will be compared to reconstructions: the *Greenspan method* [9], the *average image*, generated by composing the image with signal intensities which are the average of both the signal intensities of the slice shifted volumes, and the *composed image*, generated by composing the image with the signal intensities of both slice shifted volumes interleaved with each other (see [13] for more details).

► Analysis of the SPM activation maps. For the different reconstructed sequences, we computed the activated areas which are above the statistical threshold (pcorr < 0.05),

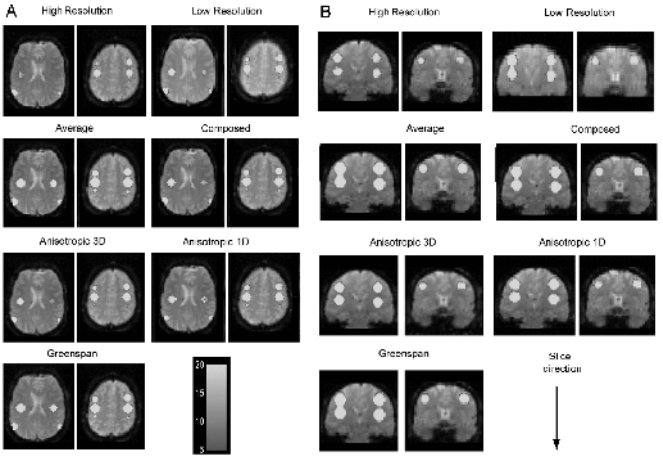

Fig. 2. Synthetic dataset: Comparison between the activated areas observed with the statistical SPM analysis in the high and low resolution datasets, and the reconstructed ones shown in the in plane (A) and through plane direction (B).

overlaid on the mean EPI images of the interpolated datasets (See figures 2 and 4). Globally all the activation maps of the interpolated datasets look largely similar to those of the high resolution reference dataset both for the synthetic as the real datasets. A closer look at the data however reveals that the superresolution datasets show higher t-values at the foci of the activated areas as compared to the reference high resolution and the original low resolution dataset especially observed in the real data. The 3D anisotropic images display more intense but less sharp activation patches as compared to the other interpolated datasets. This is the result of the larger smoothing effect inherent to the 3D anisotropic interpolation algorithm in all directions. The results obtained with the other interpolation algorithms are all very similar with a slightly higher intensity and sharper deliniation of the activated areas in the 1D anisotropic regularization case for both fMRI datasets.

► The case of closeby activated areas. We propose in figure 3 a cut through the different observed activated areas in the slice direction of the statistical maps from the synthetic dataset. These graphs show the ability of the superresolution techniques to separate 2 activated areas which are very close to each other in the slice direction. In the left graph the 2 areas are separated by 1 slice and in the right graph by 2 slices. These graphs show that the 1D anisotropic regularization method displays a much better separation capability resembling closest to the high resolution dataset as compared to the Greenspan method and both the average(not shown) and composed methods(not shown).

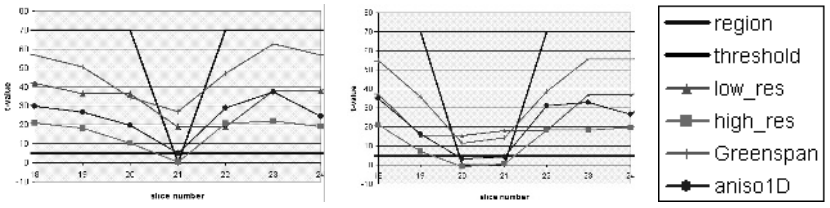

Fig. 3. Synthetic dataset: Line graphs showing the z-score values of the activated areas cutted in the slice direction for 2 activated areas separated by 1 slice (left) and 2 slices (right) in the different datasets. The real boundaries of the activated areas are shown with a blue line and the treshold of p=0.05 (corrected) is shown with a black line.

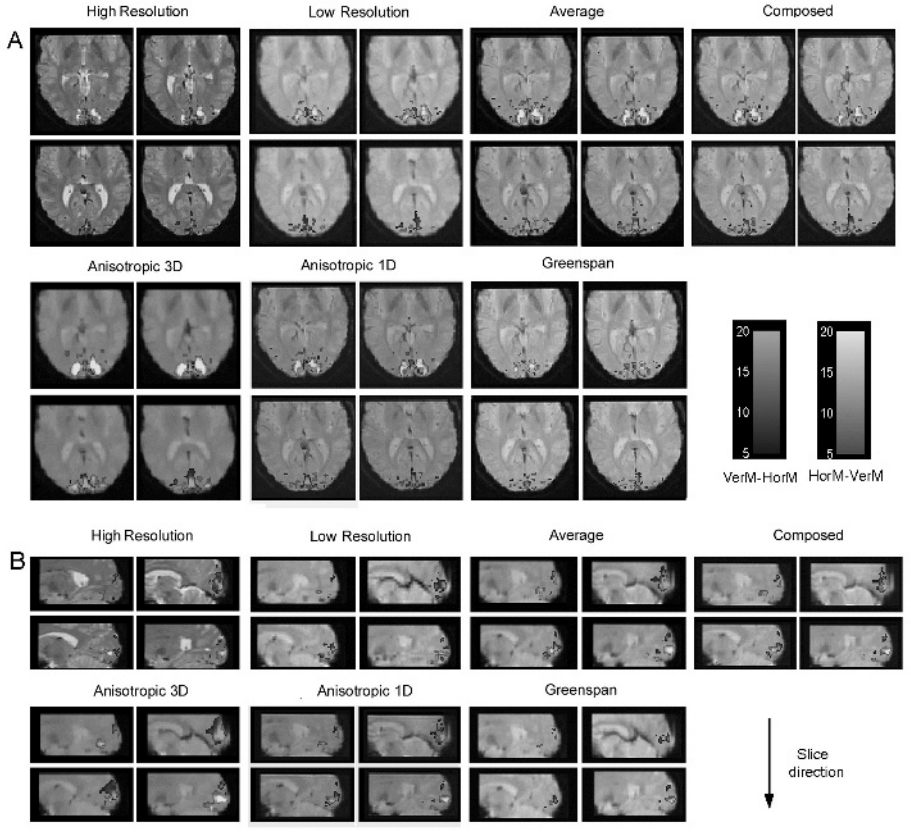

Fig. 4. Real fMRI dataset: Comparison between the activated areas for the horizontal meridian (red-yellow) and vertical meridian (blue-green) observed with the statistical SPM analysis in the original high resolution dataset, the low resolution dataset and the reconstructed datasets, shown in the in plane (A) and through plane direction (B).

5 Conclusion

This paper proposes a framework for augmenting the resolution in fMRI. It consists in settling a suitable acquisition protocol and in using some recent results from nonlinear restoration, in order to propose an efficient edge preserving superresolution algorithm. Another originality of this paper is to validate the proposed approaches using the statistical analysis of fMRI time series. A case study was first established before performing tests on a real fMRI sequence with a human volunteer. These experiments clearly establish the interest of using superresolution in this context.

Taking into account both the results of the synthetic and the real fMRI datasets we can conclude that although the 3D anisotropic diffusion superresolution dataset displays the largest activated patches it is much more smoothed in plane as compared to the 1D anisotropic superresolution and the other interpolated dataset. Therefore the algorithm with the regularization in the slice direction only (1D anisotropic) appears to be the best technique if one wants to detect small activated areas with a high resolution. On the other hand if one wants to increase detectability of large activated areas, the dataset generated with the 3D anisotropic algorithm will give the best results.

Acknowledgment. This work was partially funded by European project MAPAWAMO (QLG3-CT-2000-30161) and by RGC Grant No. HKU 7046/03P.

References

1. K. Aizawa, T. Komatsu, and T. Saito. Acquisition of very high resolution images using stereo cameras. In *SPIE Visual Communications and Image Processing*, volume 1605, pages 318–328, Boston, MA, 1991.
2. G. Aubert and P. Kornprobst. *Mathematical Problems in Image Processing: Partial Differential Equations and the Calculus of Variations*, volume 147 of *Applied Mathematical Sciences*. Springer-Verlag, January 2002.
3. G. Aubert and L. Vese. A variational method in image recovery. *SIAM Journal of Numerical Analysis*, 34(5):1948–1979, 1997.
4. D. Capel and A. Zisserman. Super-resolution enhancement of text image sequences. In *Proceedings of the International Conference on Computer Vision and Pattern Recognition*, Hilton Head Island, South Carolina, June 2000. IEEE Computer Society.
5. M. Elad and A. Feuer. Super-resolution reconstruction of continuous image sequence. *IEEE Transactions on Pattern Analysis and Machine Intelligence*, 21(9):817–834, 1999.
6. H. Engl, M. Hanke, and A. Neubauer. *Regularization of inverse problems*. Mathematics and its applications. Kluwer Academic Publishers, 2000.
7. H. Fischer and R. Ladebeck. Echo-planar imaging image artifacts. In et al. F. Schmitt, editor, *Echo-Planar Imaging, Theory, Technique and application*., pages 191–200. Springer, Heidelberg, 1998.
8. D. Geman and C. Yang. Nonlinear image recovery with half-quadratic regularization. *IEEE Transactions on Image Processing*, 4(7):932–946, 1995.
9. H. Greenspan, G. Oz, N. Kiryati, and S. Peled. MRI inter-slice reconstruction using super-resolution. *Magn. Res. Imag.*, 20:437–446, 2002.
10. F.G. Hoogenraad, M.B. Hofman, P.J. Pouwels, J.R. Reichenbach, S.A. Rombouts, and E.M. Haacke. Sub-millimeter fMRI at 1.5 Tesla: correlation of high resolution with low resolution measurements. *J Magn Reson Imaging*, 9(3):475–482, March 1999.

11. M. Irani and S. Peleg. Motion analysis for image enhancement: resolution, occlusion, and transparency. *Journal on Visual Communications and Image Representation*, 4(4):324–335, 1993.
12. D.A. Kelley and J.F. Schenck. Very-high-field magnetic resonance imaging: instrumentation and safety issues. *Top Magn Reson Imaging*, 10(1):79–89, February 1999.
13. P. Kornprobst, R. Peeters, T. Vieville, G. Malandain, S. Mierisova, S. Sunaert, O. Faugeras, and P. Van Hecke. Superresolution in MRI and its influence in statistical analysis. Technical Report 4513, INRIA, July 2002.
14. M. Nikolova and M. Ng. Fast image reconstruction algorithms combining half-quadratic regularization and preconditioning. In *Proceedings of the International Conference on Image Processing*. IEEE Signal Processing Society, 2001.
15. S. Peled and Y. Yeshurun. Superresolution in MRI : Application to human white matter fiber tract visualization by diffusion tensor imaging. *Magn. Reson. Med.*, 45:29–35, 2001.
16. E. Roullot, A. Herment, I. Bloch, M. Nikolova, and E. Mousseaux. Regularized reconstruction of 3d high-resolution magnetic resonance images from acquisitions of anisotropically degraded resolutions. In *Proceedings of the International Conference on Image Processing*. IEEE Signal Processing Society, 2000.
17. L. Rudin, S. Osher, and E. Fatemi. Nonlinear total variation based noise removal algorithms. Physica D, 60:259–268, 1992.
18. K. Sauer and J. Allebach. Iterative reconstruction of band-limited images from nonuniformly spaced samples. *IEEE Trans. Circuits Syst.*, 34:1497–1505, 1987.
19. K.R. Thulborn, S.Y. Chang, G.X. Shen, and J.T. Voyvodic. High-resolution echo-planar fMRI of human visual cortex at 3.0 Tesla. *NMR Biomed*, 10(4–5):183–90, June 1997.